nature COMMUNICATIONS

ARTICLE

https://doi.org/10.1038/s41467-020-20833-6 OPEN

A combinatory ferroelectric compound bridging simple ABO_3 and A-site-ordered quadruple perovskite

Jianfa Zhao[1,2], Jiacheng Gao[1], Wenmin Li[1], Yuting Qian[1], Xudong Shen[1,2], Xiao Wang[3], Xi Shen[1], Zhiwei Hu[3], Cheng Dong[4], Qingzhen Huang[5], Lipeng Cao[1], Zhi Li[6], Jun Zhang[1], Chongwen Ren[1], Lei Duan[1], Qingqing Liu[1], Richeng Yu[1], Yang Ren[7], Shih-Chang Weng[8], Hong-Ji Lin[8], Chien-Te Chen[8], Liu-Hao Tjeng[3], Youwen Long[1,2], Zheng Deng[1], Jinlong Zhu[9], Xiancheng Wang[1], Hongming Weng[1✉], Runze Yu[1✉], Martha Greenblatt[10] & Changqing Jin[1,2✉]

The simple ABO_3 and A-site-ordered $AA'_3B_4O_{12}$ perovskites represent two types of classical perovskite functional materials. There are well-known simple perovskites with ferroelectric properties, while there is still no report of ferroelectricity due to symmetry breaking transition in A-site-ordered quadruple perovskites. Here we report the high pressure synthesis of an A-site-ordered perovskite $PbHg_3Ti_4O_{12}$, the only known quadruple perovskite that transforms from high-temperature centrosymmetric paraelectric phase to low-temperature non-centrosymmetric ferroelectric phase. The coordination chemistry of Hg^{2+} is changed from square planar as in typical A-site-ordered quadruple perovskite to a rare stereo type with 8 ligands in $PbHg_3Ti_4O_{12}$. Thus $PbHg_3Ti_4O_{12}$ appears to be a combinatory link from simple ABO_3 perovskites to A-site-ordered $AA'_3Ti_4O_{12}$ perovskites, sharing both displacive ferroelectricity with former and structure coordination with latter. This is the only example so far showing ferroelectricity due to symmetry breaking phase transition in $AA'_3B_4O_{12}$-type A-site-ordered perovskites, and opens a direction to search for ferroelectric materials.

[1] Beijing National Laboratory for Condensed Matter Physics, Institute of Physics, Chinese Academy of Sciences; School of Physical Sciences, University of Chinese Academy of Sciences, Beijing 100190, China. [2] Songshan Lake Materials Laboratory, Dongguan 523808, China. [3] Max Planck Institute for Chemical Physics of Solids, Nothnitzer Straße 40, Dresden 01187, Germany. [4] School of Advanced Materials, Peking University Shenzhen Graduate School, Shenzhen 518055, China. [5] NIST Center for Neutron Research, National Institute of Standards and Technology, Gaithersburg 20899 MA, USA. [6] School of Materials Science and Engineering, Nanjing University of Science and Technology, Nanjing 210094, China. [7] X-ray Science Division, Advanced Photon Source, Argonne National Laboratory, Argonne 60439 IL, USA. [8] National Synchrotron Radiation Research Center, 101 Hsin-Ann Road, Hsinchu 30076, Taiwan. [9] Department of Physics, Southern University of Science and Technology, Shenzhen 518055, China. [10] Department of Chemistry and Chemical Biology, Rutgers, The State University of New Jersey, Piscataway, NJ, USA. ✉email: hmweng@iphy.ac.cn; yurz@iphy.ac.cn; Jin@iphy.ac.cn

Perovskites and their derivatives show many interesting physical, chemical and mineral properties such as ferromagnetism, ferroelectricity, piezoelectricity, ion conductivity, photocatalysis and superconductivity[1–18] that can be modified dramatically by the coordination chemistry for a given composition. There is a special class of perovskite-type materials with the general chemical formula $AA'_3B_4O_{12}$, named A-site-ordered, or quadruple perovskites, which received much attention owing to their fascinating structural and wide varieties of physical properties[10], including colossal magnetoresistance under weak field[11], charge disproportionation[12] and giant dielectric constant over a wide temperature range[13,14]. For the simple ABO_3 perovskite, the 12-fold coordinated A-site is often occupied by large size ions such as alkali metal, alkaline earth or lanthanide cations and the 6-fold coordinated B-site is often occupied by transition metals (TMs) to satisfy the so called tolerance factor $t = (r_A + r_O)/\sqrt{2}(r_B + r_O)$ (r_A, r_B, & r_O represent for the ion radius of A, B, and O, respectively) with t usually in the range of 0.75 to 1.05 for stable perovskite compounds[1,18]. However in the A-site-ordered perovskite $AA'_3B_4O_{12}$, three quarters of the A-site is substituted by a TM, A′ with much smaller ionic radius[16–19]. Generally, TM ions with strong Jahn-Teller distortions like Mn^{3+} and Cu^{2+} preferentially occupy the A′-site with square-planar coordination[20–24]. The small TM ion at the A′-site causes the distortion of BO_6 octahedron in $AA'_3B_4O_{12}$ perovskite, usually resulting in a cubic crystal structure with space group *Im*-3[25]. From a structural point of view, the flexibility for tilting the BO_6 octahedra in $AA'_3B_4O_{12}$ perovskite is limited in order to maintain the square-planar coordination at the originally 12-fold coordinated A-site in the simple perovskite structure[21].

Ferroelectricity is one of the most important properties for application in actuators, sensors, and memory storage devices, etc. Large numbers of ferroelectric materials possess simple perovskite structures, such as $BaTiO_3$, $PbTiO_3$, Pb(Ti, Zr)O_3, $BiFeO_3$[26–30]. The origin of ferroelectricity is due to either the lone pair $6s^2$ effect of cations (Pb^{2+}, Bi^{3+}), or the second-order Jahn-Teller active cations with electron configuration of d^0 (Ti^{4+}, Zr^{4+}); these compounds are usually referred to as displacive-type ferroelectrics. However, ferroelectricity is seldom observed in $AA'_3B_4O_{12}$ type A-site-ordered compounds, even when they contain second-order Jahn-Teller active cations or lone pair effect cations[28]. One reason for the absence of ferroelectricity in this series of compounds is the usual presence of a centrosymmetric structure, and the variation of temperature generally causes isostructural or centrosymmetric - to - centrosymmetric phase transition[12,21,25], hence there cannot be spontaneous polarization. Currently the rare examples in this series that show ferroelectricity are AMn_7O_{12} (A = Ca, Bi or Pb)[31–33] and $AMn_3Cr_4O_{12}$ (A = La or Bi)[20,22]. Although these compounds have centrosymmetric structures, all are spin-driven multiferroic systems, due to strong magnetoelectric coupling effects[20,22,32]. Up to now, there is still no report of ferroelectricity from symmetry breaking transition in A-site-ordered perovskite compounds.

In this work, an $AA'_3B_4O_{12}$ type A-site-ordered perovskite oxide, $PbHg_3Ti_4O_{12}$ (henceforth PHTO) was designed and synthesized at high pressure and high temperature conditions. It is found that the Hg^{2+} ion occupies the A′-site in $AA'_3B_4O_{12}$ type perovskite in sharp contrast to previous reports where 3*d* TM ions (Cu^{2+}, Mn^{3+}) usually locate at the A′-site. Moreover, ferroelectricity was observed in PHTO, when its ambient centrosymmetric phase transformed to a non-centrosymmetric phase at 250 K. The origins of ferroelectricity are discussed based on the comprehensive characterizations of crystal structure using both neutron and synchrotron x-ray diffractions and density functional theory (DFT) calculation.

Results and Discussion

Crystal structure. The NPD refinements are shown in Fig. 1a, which confirm that PHTO crystallizes in the $AA'_3B_4O_{12}$ type A-site-ordered perovskite. The refined structure parameters of PHTO based on NPD data collected at 295 K are listed in Table 1. No anomaly is observed in the occupation parameters at any site, including full occupancy for the oxygen site as well. Thus, PHTO should have stoichiometric composition. Bond valence sum (BVS) calculations based on the refined structure from NPD data give valences of +2.26 for Pb ions, +1.99 for Hg ions and +3.88 for Ti ions (see Table 1), which are consistent with x-ray absorption spectroscopy (XAS) results discussed later. Hence the obtained sample is an A-site-ordered perovskite with stoichiometric $Pb^{2+}Hg^{2+}{}_3Ti^{4+}{}_4O_{12}$ formula and space group *Im*-3 as shown in Fig. 1b. The structure model is consistent with the refinements of SXRD data as shown in Supplementary Fig. S1 and Table S1. Moreover, for Hg ions, if

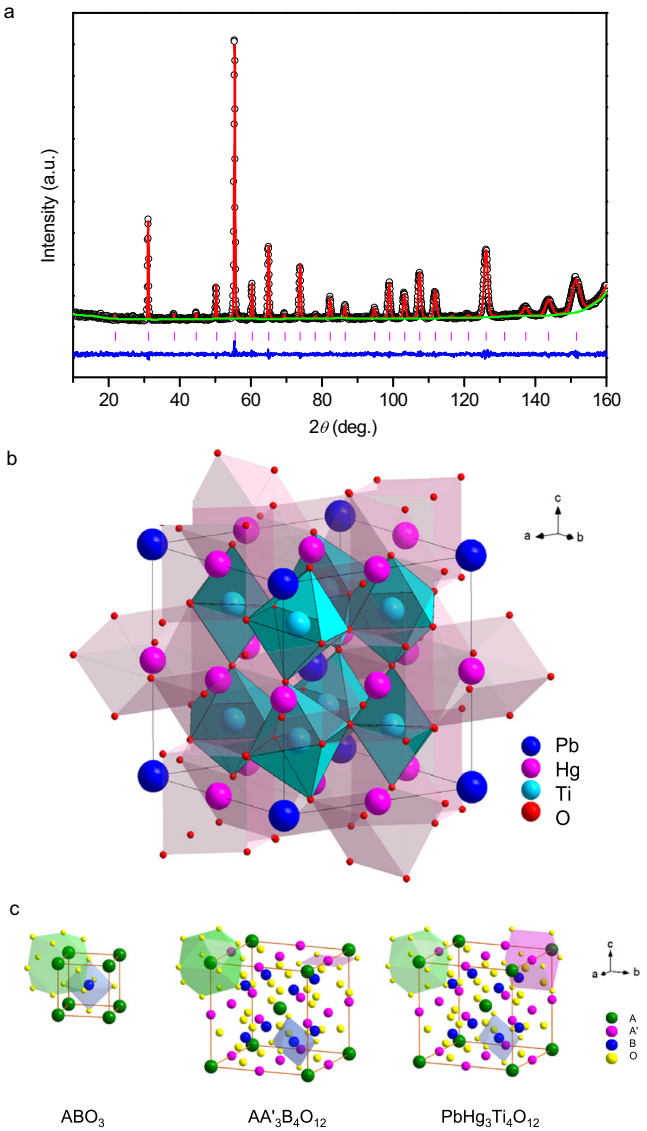

Fig. 1 Neutron diffraction and crystal structure of PHTO. a Rietveld refinements based on NPD data at 295 K. Observed (crosses), calculated (red), difference (blue) are shown in the figure, respectively. The ticks indicate the allowed Bragg reflections with space group *Im*-3. **b** Crystal structure of PHTO. **c**, Schematic coordination of A, A′ and B-site for ABO_3, $AA'_3B_4O_{12}$ and $PbHg_3Ti_4O_{12}$ respectively.

Table 1 Refined structure parameters of PHTO based on NPD data collected at 295 K.

	NPD
a(Å)	7.7283(2)
Z	2
Formula weight (g/mol)	1192.56
Cacl. Density (g/cm^3)	8.5800(2)
V(Å^3)	461.57(9)
O_y	0.7155(1)
O_z	0.2090(7)
U_{iso}(Pb)(Å^2)	0.009(5)
U_{iso}(Hg)(Å^2)	0.014(2)
U_{iso}(Ti)(Å^2)	0.010(0)
U_{iso}(O)(Å^2)	0.014(0)
Pb-O(×12)(Å)	2.728(5)
Hg-O(×4)(Å)	2.320(5)
Hg-O(×4)(Å)	2.798(1)
Ti-O(×6)(Å)	1.975(8)
∠Ti-O-Ti (°)	155.83(6)
BVS(Pb)	2.26
BVS(Hg)	1.99
BVS(Ti)	3.88
R_{wp}(%)	4.56
R_p(%)	4.12

The BVS values (V_i) were calculated using the formula $V_i = \Sigma_j S_{ij}$, and $S_{ij} = \exp[(r_O - r_{ij})/0.37)]$. In PHTO, $r_O = 2.112$ for Pb, 1.972 for Hg and 1.815 for Ti. For the A-site Pb, 12-coordinated oxygen atoms were used. For the A′-site Hg, 8-coordinated oxygen atoms were used. For the B-site Ti, 6-coordinated oxygen atoms were used. [b]Space group: *Im*-3; Atomic sites: Pb 2*a* (0, 0, 0), Hg 6*b* (0, 0.5, 0.5), Ti 8*c* (0.25, 0.25, 0.25), O 24*g* (0, *y*, *z*).

Table 2 Lattice constant *a*, ionic radius of A-site r_A, ionic radius of A′-site $r_{A'}$, difference between ionic radii of A- and A′-site ions Δr_A, metal−oxygen bond angles ∠A′−O−Ti and ∠Ti−O−Ti for some $AA'_3Ti_4O_{12}$ type perovskite compounds[33].

Compounds	*a*/Å	r_A/Å	r_A/Å	Δr_A/Å	∠A′−O−Ti/deg	∠Ti−O−Ti/deg
$PbHg_3Ti_4O_{12}$	7.7234	1.49	0.96	0.53	102.60	154.22
$CaPd_3Ti_4O_{12}$	7.4977	1.34	0.64	0.70	107.17	144.93
$CaFe_3Ti_4O_{12}$	7.4672	1.34	0.64	0.70	107.82	144.01
$CaCu_3Ti_4O_{12}$	7.3730	1.34	0.57	0.77	108.98	141.33
$SrCu_3Ti_4O_{12}$	7.4275	1.44	0.57	0.87	109.18	141.21

one considers the four nearest - neighbor O atoms (Hg-O(×4) = 2.320(5) Å), the BVS value is only 1.56. However, if one takes into accounts the four next - nearest - neighbor O atoms (Hg-O (×4) = 2.798(1) Å) additionally, the BVS value is 1.99. Therefore, Hg ions at A′-site are close to 8 -coordinated by O, in sharp contrast to typical A-site-ordered perovskite where the A′-site is usually 4-coordinated by O (See Fig. 1c). Note that, the PHTO sample is single phase of high quality, no detectable diffraction peak belonging to $PbTiO_3$ or $HgTiO_3$ was found in either NPD or SXRD patterns.

As aforementioned, usually the strong Jahn-Teller active ions, like Cu^{2+} and Mn^{3+}, are preferentially accommodated into the square-coordinated A′-site in the A-site-ordered perovskites, as in $LaCu_3Fe_4O_{12}$ and $BiMn_3Cr_4O_{12}$[20,21]. Some other TM ions have been recently introduced at the A′-site such as in $CaCo_3V_4O_{12}$[34], $CaFe_3Ti_4O_{12}$[35], $CaPd_3Ti_4O_{12}$[36]. Thus PHTO is an $AA'_3B_4O_{12}$ type perovskites with the A′-site fully occupied by Hg^{2+}, other than 3*d* TM, or Pd as shown in Table 2. The lattice parameter (7.72 Å) of PHTO is larger compared to those of other $AA'_3B_4O_{12}$ type

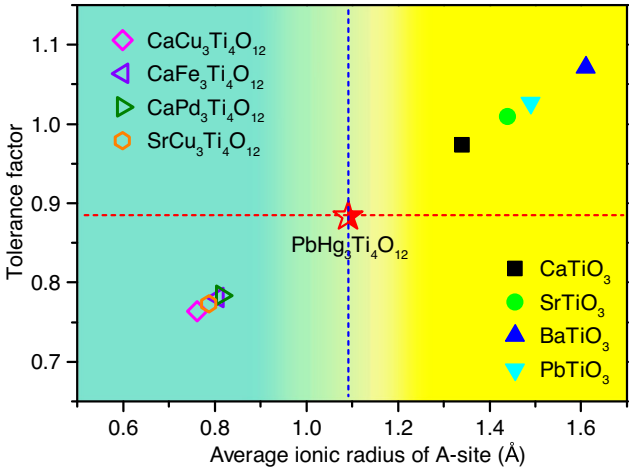

Fig. 2 Tolerance factor *t* versus average ionic radius of A-site for simple perovskites $ATiO_3$ and A-site-ordered perovskites $AA'_3Ti_4O_{12}$. Upper right panel is the area for simple $ATiO_3$ perovskites; Lower left panel is the area for $AA'_3Ti_4O_{12}$ perovskites; The middle point is PHTO.

perovskites (7.3–7.5 Å), while the ∠Ti–O–Ti angle (155.8°) of PHTO is less distorted from the ideal 180° than those for other $AA'_3B_4O_{12}$ type perovskites ($\angle B\text{–}O\text{–}B \approx 140°$). The larger ∠Ti–O–Ti angle and correspondingly smaller ∠A′−O−Ti angle in PHTO imply the less tilting of TiO_6 octahedron, which is attributed to the large ionic size of Hg^{2+} about 0.96 Å. Figure 2 shows the tolerance factor *t* versus average ionic radius of A-site ions for simple perovskites $ATiO_3$ and A-site-ordered perovskites $AA'_3Ti_4O_{12}$ where the *t* factor is calculated assuming a simple ABO_3 form with the average ionic size at A site. It is found that from $CaTiO_3$ to $BaTiO_3$, the ionic radius of A-site increases from 1.34 Å to 1.61 Å while the tolerance factor *t* increases from 0.97 to 1.07. The simple perovskites $ATiO_3$ are located at the upper right panel of Fig. 2. For most of the $AA'_3Ti_4O_{12}$ compounds, the average ionic radius of A-site is about 0.8 Å and the tolerance factor *t* is around 0.77. Therefore, $AA'_3Ti_4O_{12}$ perovskites are located at the lower left panel of the Fig. 2. However, different from these $ATiO_3$ and $AA'_3Ti_4O_{12}$ compounds, the average ionic radius of A-site ion for PHTO is large, about 1.1 Å and the tolerance factor *t* is about 0.88. Moreover as aforementioned, the coordination number for Hg ions at the A′-site in PHTO is eight, not square planar as in A′-TM quadruple perovskites $AA'_3Ti_4O_{12}$, and it is located in the middle area of Fig. 2, between those of simple $ATiO_3$ (coordination number 12) and $AA'_3Ti_4O_{12}$ quadruple perovskites (coordination number 4). Thus, PHTO appears to be a link from simple $ATiO_3$ perovskite to $AA'_3Ti_4O_{12}$ type A-site-ordered perovskite (Fig. 2). The A-site coordination number for ABO_3 perovskite is 12 while the A-site and A'-site coordination numbers in the A-site-ordered quadruple perovskite $AA'_3B_4O_{12}$ compound are 12 and 4 respectively. However in PHTO, the coordination number of A′ (Hg^{2+}) is 8, which is just in between that for simple $ATiO_3$ and $AA'_3Ti_4O_{12}$. This result provides further evidence supporting the scenario aforementioned. Considering that the ionic size of Sr^{2+} (1.45 Å) is similar to that Pb^{2+} (1.49 Å), we also fabricated the A-site-ordered perovskite compound $SrHg_3Ti_4O_{12}$, which is isostructural with PHTO, but without the observation of ferroelectricity. The result about $SrHg_3Ti_4O_{12}$ will be published elsewhere. According to the previous report[37], the low energy level of d^{10} orbital prefers a relatively high coordination number owing to the weak *d*-*s* and *d*-*p* hybridization in perovskite compounds. As to PHTO system, the first principles calculation result indicates that the energy level

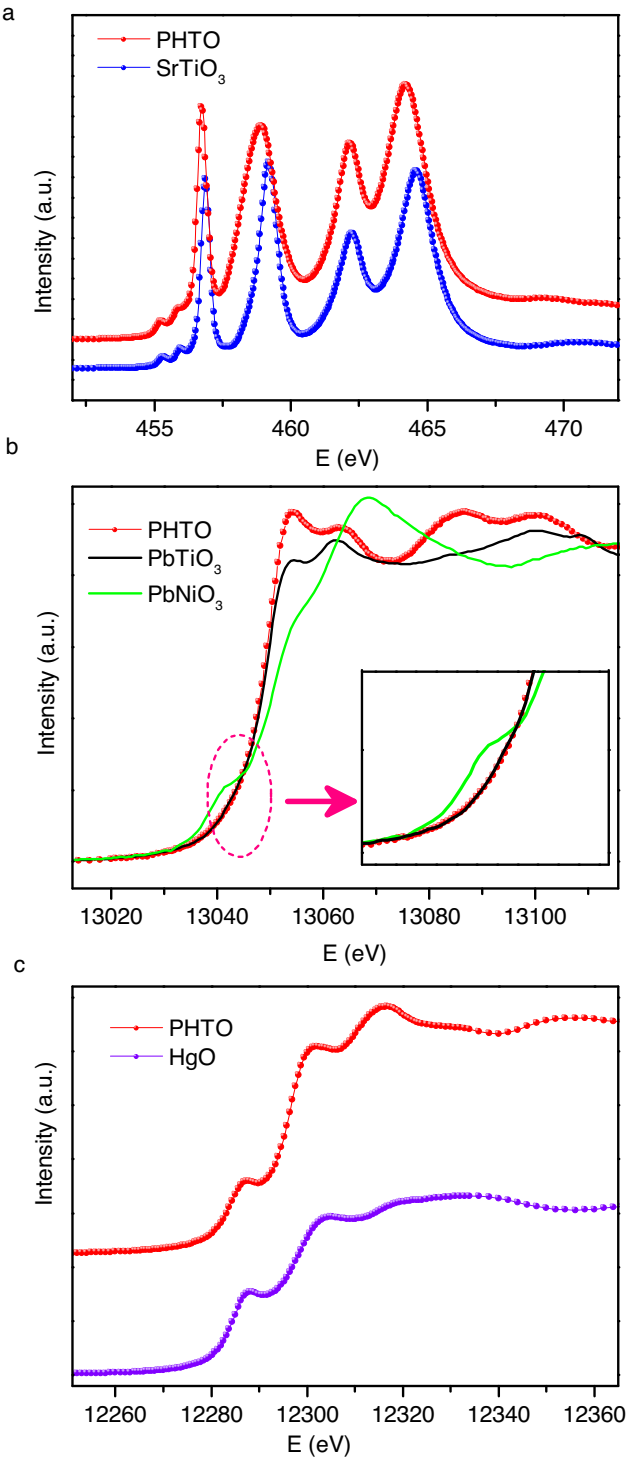

Fig. 3 X-ray absorption spectroscopy of PHTO. a Ti-$L_{2,3}$ edge. **b** Pb-L_3 edge. **c** Hg-L_3 edge.

of d^{10} for Hg^{2+} has a lower energy for 8 coordination than that for 4 coordination (See Supplementary Fig. S2a). Moreover PHTO also shows a low total energy in the state of 8 coordination of Hg^{2+} (See Supplementary Fig. S2b). Thus 8-fold coordination of Hg^{2+} is more stable than 4-fold in the PHTO system.

Valence state analysis. Soft X-ray absorption spectroscopy at the $L_{2,3}$ edge of TM *3d* ions[38] is a highly sensitive method to determine the valence state[39,40], local environment[41], and orbital occupation[42] of the ions. Figure 3a shows the Ti-$L_{2,3}$ XAS spectra of PHTO together with $SrTiO_3$ as a pure Ti^{4+} reference. The very similar multiplet spectral features in PHTO and $SrTiO_3$ clearly correspond to the Ti $2p^63d^0 \rightarrow 2p^53d^1$ transition[43,44], demonstrating the Ti^{4+} valence state in PHTO. Note that the PHTO spectrum is shifted by about 0.25 eV to lower energy with respect to the $SrTiO_3$ spectrum, reflecting the different Ti local environments. Actually the Ti-O distance is 1.974(7) Å in PHTO and 1.951(7) Å in $SrTiO_3$[45], which suggests a weaker crystal field effect in PHTO. Figure 3b shows the Pb-L_3 XAS spectra of PHTO together with $PbTiO_3$ as a Pb^{2+} and $PbNiO_3$ as Pb^{4+} reference. The weak pre-edge feature in $PbNiO_3$ due to excitation from a *2p* core electron to the *6s* orbital. It has been established that this weak pre-edge feature is a sensitive finger-print of the Pb valence state in solid state materials[46]. The reason is that the Pb $5d^{10}$ orbitals are fully occupied, the valence state is then reflected by the *6s* occupation. However, as shown in the inset, PHTO has the Pb-L_3 XAS profile similar to the Pb^{2+} reference $PbTiO_3$ in detail, no *2p*–*6s* related excitation is observed in PHTO, which indicates the valence state of Pb^{2+} with fully occupied $6s^2$ state in this compound. Figure 3c shows the Hg-L_3 XAS spectra of PHTO as well as HgO. The same energy position and very similar spectral profile of both PHTO and HgO indicate the Hg^{2+} valence state. The XAS results show that the electronic configuration of PHTO is $Pb^{2+}Hg^{2+}{}_3Ti^{4+}{}_4O_{12}$, which is fully consistent with the BVS results based on the crystal structure.

Magnetic and transport characterizations. The magnetic susceptibility χ is almost constant and negative near zero from 300 K to 30 K, while χ increases rapidly on further decrease of temperature as shown in Supplementary Fig. S3. These results revealed that PHTO is nonmagnetic due to the $3d^0$, $5d^{10}$ and $6s^2$ electron configuration for Ti^{4+}, Hg^{2+} and Pb^{2+}, respectively, and consistent with the BVS calculations and XAS results. The resistance of PHTO at room temperature is too large to be measured, indicating the high electrical insulating property and few vacancies in the sample. Supplementary Fig. S4a shows the Ultraviolet-Visible-Near Infrared (UV-Vis-NIR) absorption spectrum of PHTO. The curve exhibits a steep decrease from 420 to 640 nm, which is a typical optical response of semiconductors. The optical band gap of the PHTO was estimated to be 2.12 eV. The first principles calculations show that PHTO is a direct gap insulator with 1.70 eV gap at the *H* point shown in Supplementary Fig. S4b. The gap might be underestimated in DFT calculations, nevertheless, it reveals the wide gap nature of PHTO. The obtained PHTO sample is stable at ambient up to 973 K as revealed by thermogravimetry analysis measurements shown in Supplementary Fig. S5.

Dielectricity and ferroelectricity. The permittivity and dielectric loss measured with different frequencies from 2 K to 300 K are shown in Fig. 4a, b, respectively. The relative dielectric constant, ε_r of PHTO is over 220 in the measured temperature range. The temperature dependence of ε_r shows a clear peak around 250 K at all the frequencies of measurements. The overall temperature-dependent ε_r strongly indicates a low-temperature ferroelectric phase transition to a high-temperature paraelectric phase at $T_{FE} \approx 250$ K. Furthermore, the transition temperature is independent of measurement frequency, indicating that PHTO is not a relaxor-type ferroelectric material. The relative increase of the dielectric loss around 250 K is consistent with the paraelectric-ferroelectric transition. Moreover the dielectric loss keeps at a very low value (<0.03) with all of frequency in the whole measurement range, which indicate the intrinsic dielectric property of

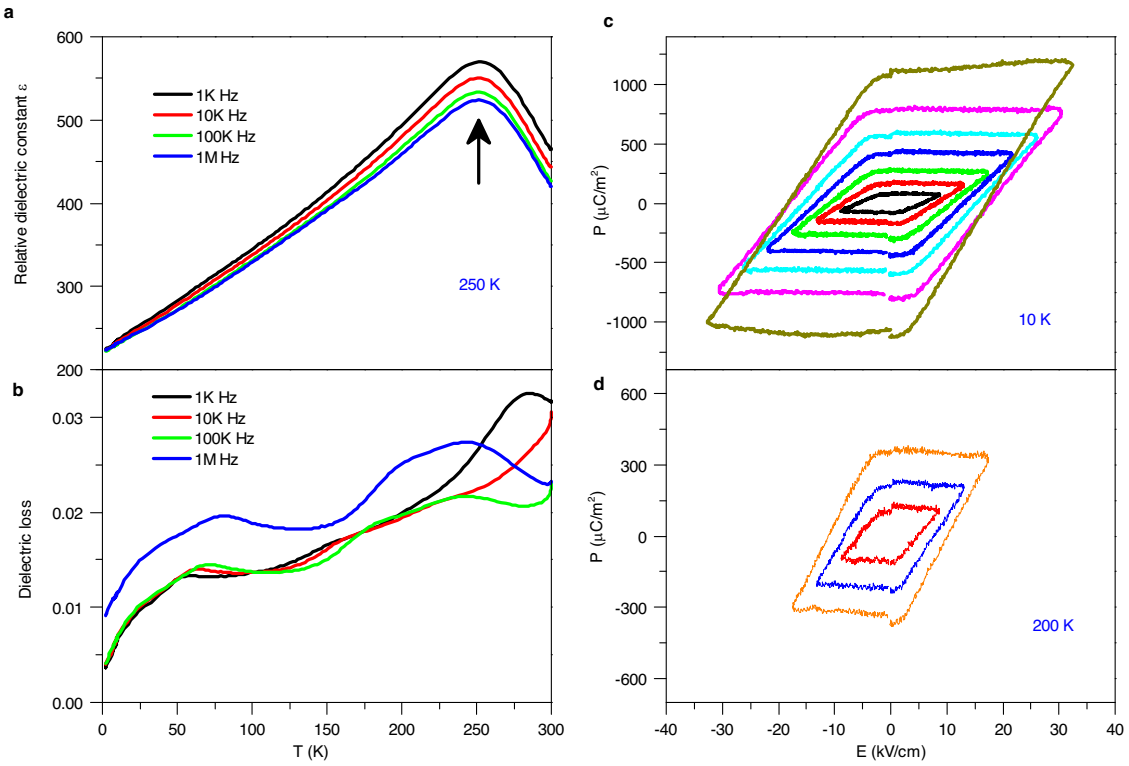

Fig. 4 Dielectricity and ferroelectricity of PHTO. Temperature dependence of **a** relative dielectric constant ε_r, and **b** dielectric loss at selected frequencies. The *P*–*E* hysteresis loops measured at **c** 10 K and **d** 200 K under selected electric fields.

PHTO. In order to further identify the ferroelectricity of PHTO, the isothermal polarizations were measured by the PUND method[20]. No loops of polarization versus electric field (*P*–*E*) were observed in polycrystalline PHTO at room temperature. However, canonical *P*–*E* hysteresis loops were observed below 250 K as shown in Fig. 4c, d. It is clear that polarization is enhanced at low temperature. At fixed temperature, the *P*–*E* loops significantly expand with increasing electric field. For example, the *P* value increases from 0.028 to 0.11 μC cm^{-2} as the maximum electric field changes from 17 to 32 kV cm^{-1} at 10 K. As known, $PbTiO_3$ is a classic and extensively studied ferroelectric material with Curie temperature about 763 K, which excludes the possibility that the ferroelectricity of PHTO originated from $PbTiO_3$. Thus it can be concluded that the ferroelectricity is due to PHTO.

Temperature dependent crystal structure transition. To further understand the mechanism of ferroelectricity from the structure point of view, we performed the temperature dependent SXRD, as shown in Supplementary Fig. S6. The characteristic (400) diffraction peak at different temperatures is collected in Fig. 5a. It is obvious that the diffraction peaks split into two sub-peaks between 240 K and 260 K, which indicates the occurrence of temperature induced phase transition at 250 K is due to symmetry reduction from a cubic - to - orthorhombic phase. Checking the SXRD data measured at 300 K and 90 K, all the high symmetry diffraction peaks, such as (200), (220), (222), (400) and (402) of the high temperature phase, are split into two sub-peaks on cooling to low temperature (see Supplementary Fig. S7). There is a clear long-range structural transition with decreasing temperature. The SXRD data collected at 90 K is presented in Fig. 5b. The crystal structure of PHTO can be fitted very well by an orthorhombic phase of non-centrosymmetric space group *Imm*2 (No.44). The inset shows the crystal structure of the low temperature phase. The Rietveld refinement results are listed in Supplementary Table S2. Figure 5c shows variation of the lattice parameters based on refinements of SXRD data. The lattice parameter *a* decrease lineally from 300 K to 250 K. Below the temperature of the phase transition, the lattice parameter *b* and *c* continue to decrease while parameter *a* increases. Figure 5d shows the evolution of TiO_6 octahedron before and after phase transition. In the high temperature phase, TiO_6 forms a regular octahedron with ∠Ti–O–Ti angle of 155.8° and Ti-O bond length of 1.974 Å respectively. When this cubic phase transformed to an orthorhombic non-centrosymmetric phase below 250 K, both ∠Ti–O–Ti angles and Ti-O bond lengths divergences occurred in TiO_6 octahedron. These distortions originate from the relative displacements of Ti and O around all the axis directions. The polarization in the *ab*-plane was canceled due to the random relative displacements of Ti and O, leaving the polarization vector only along the [001] direction. As to HgO_8 polyhedron, the single type HgO_8 polyhedron with only two-types of Hg-O bond length in the high temperature phase evolves into three different type of HgO_8 polyhedron with different bond length in the low temperature phase, but without contribution to the polarization. Supplementary Fig. S8 illustrates the evolution of HgO_8 during the paraelectric-ferroelectric transition. Therefore, PHTO is a displacive-type ferroelectric. The ionic spontaneous polarization can be calculated by multiplying the effective charges and the distance between the negative and positive valence weighted mean center along the *c*-axis then divided by the volume of the unit cell[47]. Based on the refined results of NPD data collected at 5 K in Table 3, the calculated polarization value is about 13.65 μC cm^{-2}. Although temperature-dependent phase transition is typical in A-site-ordered perovskites, it is usually isostructural or centrosymmetric - to - centrosymmetric phase transition

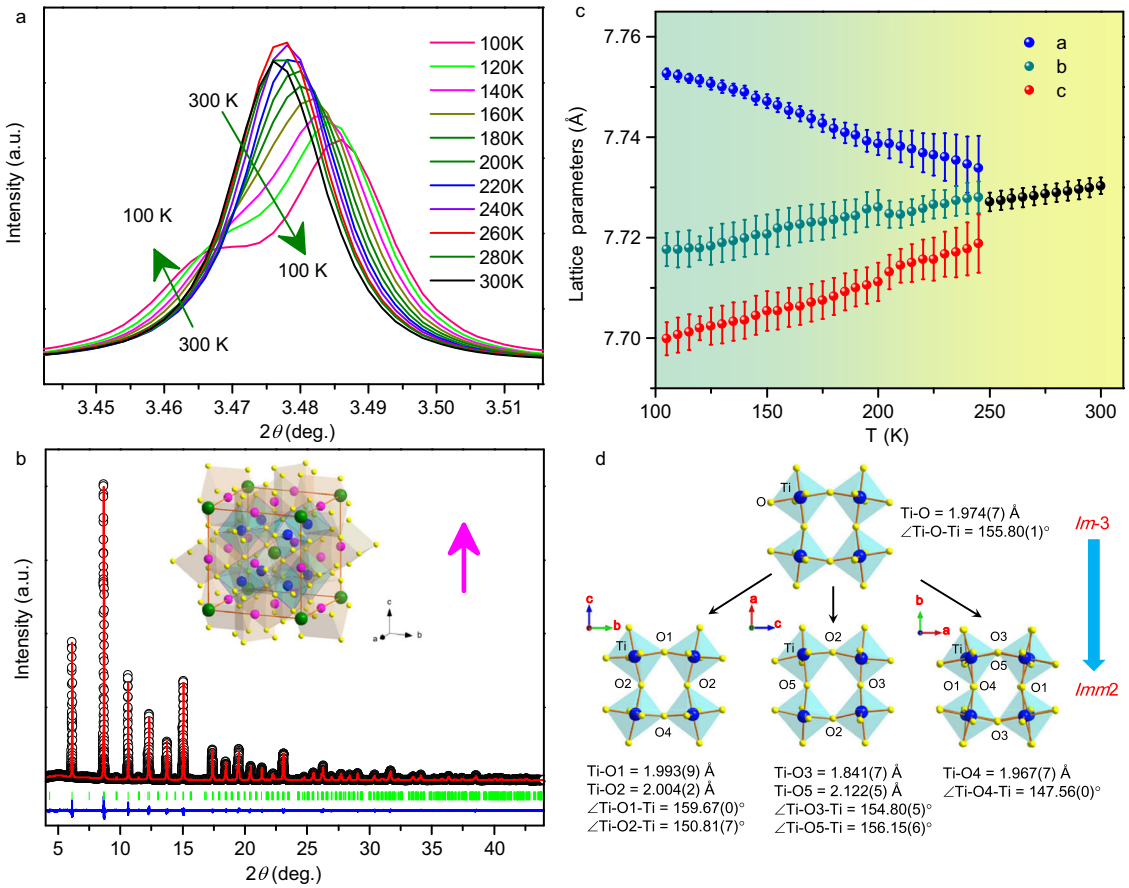

Fig. 5 Temperature induced structural transition in PHTO. a The characteristic diffraction peaks (400) collected at different temperatures. **b** Rietveld refinements based on SXRD data at 90 K. The arrow denotes the polarization direction. **c** Temperature dependence of the lattice constant and **d** schematic illustration for the changing of TiO_6 octahedron along different axis.

Table 3 Refined structure parameters of PHTO based on NPD data collected at 5 K.

Crystallographic data for $PbHg_3Ti_4O_{12}$ based on NPD at 5 K

Atom	Wyck	x	y	z	U_{iso} (Å^2)
Pb	2a	0.5	0.5	0.5	0.008(8)
Hg1	2b	0.5	0	0.5	0.007(1)
Hg2	2a	0.5	0.5	0	0.005(1)
Hg3	2b	0.5	0	0	0.005(4)
Ti	8e	0.2353(7)	0.2396(3)	0.2455(8)	0.013(9)
O1	4c	0.1966(0)	0	0.2905(6)	0.007(0)
O2	8e	0.2786(9)	0.2103(7)	0.0006(9)	0.013(4)
O3	4d	0	0.2802(5)	0.2527(9)	0.027(0)
O4	4c	−0.2008(6)	0	−0.3022(4)	0.025(1)
O5	4d	0	−0.2696(8)	−0.1963(7)	0.022(2)
Bond length (Å)				**Bond angle(°)**	
Pb-O1: 2.708(6)	Ti-O1: 1.901(8)		Hg1-O1: 2.853(4)	∠Ti-O1-Ti: 152.07(9)	
Pb-O2: 2.701(6)	Ti-O2: 2.005(6)		Hg1-O3: 2.580(1)	∠Ti-O2-Ti: 157.85(3)	
Pb-O3: 2.907(2)	Ti-O3: 1.853(2)		Hg1-O5: 2.331(4)	∠Ti-O3-Ti: 160.25(5)	
Pb-O4: 2.801(7)	Ti-O4: 2.098(0)		Hg2-O1: 2.220(1)	∠Ti-O4-Ti: 145.80(6)	
Pb-O5: 2.569(6)	Ti-O5: 2.102(0)		Hg2-O2: 2.814(7)	∠Ti-O5-Ti: 155.11(8)	
			Hg2-O4: 2.179(1)		
			Hg3-O2: 2.360(5)		
			Hg3-O3: 2.547(8)		

Space group: *Imm*2 (No. 44) $a = 7.7568(9)$ Å, $b = 7.7040(1)$ Å, $c = 7.7019(8)$ Å; $\alpha = \beta = \gamma = 90°$; $V = 460.26$ Å^3; $Z = 2$; $R_p = 4.08\%$, $R_{wp} = 3.39\%$.

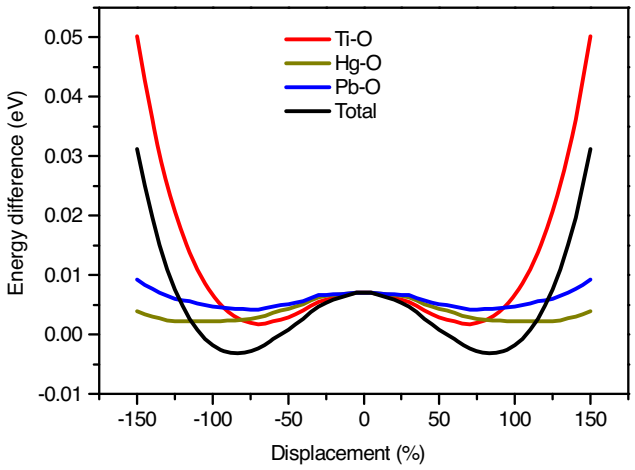

Fig. 6 First principles calculation results of the energy changes with respect to the different moving mode along one of the soft mode on Γ point. The red, yellow, blue lines correspond to Ti-O displacements only, Hg-O displacements only and Pb-O displacements only. The black line corresponds to all atoms displacements. The double well structure of the graph indicates the spontaneous structure phase transition.

from *Im*-3 to *Pn*-3. Most of those phase transitions are mainly induced by charge transfer between the A′-site and B-site ions or charge disproportionation at B-site ions[12,21,25]. PHTO is an example of $AA'_3B_4O_{12}$ type A-site-ordered perovskite that exhibits a centrosymmetric to non-centrosymmetric phase transition.

First principles calculations. In order to get a deeper insight into the ferroelectricity of PHTO at low temperature, first principles calculations have been performed. Supplementary Fig. S9 shows the phonon spectrum for the cubic structure of PHTO: three imaginary frequency modes with irreducible representation T_u degenerate at Γ point. By moving atoms along these soft phonon modes, the non-centrosymmetric crystal structure with space group *Imm*2 can be obtained. Free energy per primitive cell versus moving amplitude of atoms along one of the soft modes is plotted in Fig. 6. The energy well suggests a spontaneous structure phase transition with the biggest contribution coming from the Ti-O mode. The imaginary modes at *H* point only consist of the Ti-O phonon modes, which are consist with the experimental conclusion. In addition, the $6s^2$ lone pair electrons of Pb^{2+} also contribute to the site instability according to the theory analysis. However, the contribution from the lone pair mechanism does not play a dominant role from the energy perspective (see Fig. 6). Using Berry phase method, the polarization of ferroelectric structure and Born effective charge have been calculated. The calculated polarization value is about 16.87 μC cm^{-2}, which can also be obtained by multiplying the Born effective charge tensor with the corresponding atom displacements. This result is roughly in agreement with that ionic spontaneous polarization calculation result of 13.65 μC cm^{-2} based on neutron diffraction measurements. Both values are larger than the experimental result. This is because the calculated value is based on single crystal data, while the experimental measured value is from a polycrystalline sample of randomly distributed grains. For example, in ceramic samples of $BiFeO_3$, much lower values of about 8.9 μC cm^{-2} of polarization have been measured at room temperature while in single crystals the polarization is up to 60 μC cm^{-2} along [012] axis and 100 μC cm^{-2} along [001] axis[48,49]. Another reason for the low experimental value of polarization may be due to the grain boundary effect and/or leaking current issue preventing the application of maximum electric field in the experiment[48,50]. Supplementary Fig. S10 shows the SEM image of the polycrystalline sample of PHTO. It can be seen that the grain size distributes around several microns to nearly 20 microns and generates a large amount of grain boundaries. Those grains are disorderly distributed, which will severely affect the polarization.

The A-site-ordered perovskite $PbHg_3Ti_4O_{12}$ was synthesized at high pressure and high temperature. $PbHg_3Ti_4O_{12}$ is a nonmagnetic insulator with a direct energy gap of ~2.12 eV and relative dielectric constant larger than 220. $PbHg_3Ti_4O_{12}$ undergoes a transition from a high temperature centrosymmetric, cubic and paraelectric phase to a low temperature non-centrosymmetric, orthorhombic and ferroelectric phase with a record high Curie temperature at 250 K for an A-site-ordered quadruple perovskite. The ferroelectric distortion is dominated by Ti-O phonon mode anomaly. Because of the large average size of the A-site cation ~ 1.1 Å in PHTO, the coordination of Hg^{2+} is not square planar as in typical A-site-ordered quadruple perovskites, but closer to 8. Therefore PHTO can be considered to be structurally linking ABO_3 simple and $AA'_3B_4O_{12}$ quadruple perovskites. The established A-site-ordered perovskites $AHg_3B_4O_{12}$ may provide a potential pathway to find a class of ferroelectric materials of high Curie temperature. The work provides one of unique examples that high pressure synthesis can lead to the compounds with unique properties that are otherwise hard to get access at ambient. Moreover perovskites are the most abundant minerals in the broad lower Mantle of the Earth where high pressure is prevailing. Hence it might shed lights to further understand the coordination chemistry of perovskites like compounds at high pressures.

Methods

Sample fabrication. The polycrystalline sample of PHTO was synthesized by a solid state reaction under high pressure of 6 GPa and high temperature of 1273 K. The starting materials HgO (Aldrich, 99.0% pure), PbO (Alfa, 99.995% pure) and TiO_2 (Alfa, 99.995% pure) were mixed homogenously in a molar ratio 1:3:4 and pressed into a pellet with diameter of 6 mm in an argon gas protected glove box with oxygen and H_2O level of less than 1 ppm. The pre-pressed pellet was sealed in a gold capsule. High pressure experiments were performed with the cubic anvil type high pressure apparatus[51,52]. After the pressure was gradually increased to 6 GPa, the sample was heated to 1273 K and maintained for 30 min. Then the temperature was quenched to ambient before the release of pressure. In this process, yellow polycrystalline PHTO was obtained.

Structure characterization. The crystal structure was characterized by neutron powder diffraction (NPD) with the BT-1 high-resolution neutron powder diffractometer with a Ge (311) monochromator at the Center for Neutron Research (NCNR) of the National Institute of Standard & Technology (NIST). The neutron wavelength was 2.0774 Å. The intensities were measured with steps of 0.05° in the 2θ range of 10°–160°. The sample was also measured by synchrotron x-ray diffraction (SXRD) at the 11-BM-B at the Advanced Photon Source (APS) in Argonne National Laboratory. The X-ray wavelength was 0.412726 Å. Diffraction data were collected in the angle (2θ) range from 0.5° to 50° with steps of 0.002°. The obtained NPD and SXRD data were analyzed by the Rietveld method with the GSAS program[53].

Valences determination. The valence states of the Ti, Pb and Hg ions were determined by x-ray absorption spectroscopy (XAS). The soft XAS at the Ti-$L_{2,3}$ edge was measured with total the electron yield mode at the Dragon beamline while the hard XAS at the Pb-L_3 and Hg-L_3 edge were measured with transmission geometry at the BL07A beamline at National Synchrotron Radiation Research Center (NSRRC) of Taiwan. $SrTiO_3$, $PbTiO_3$, $PbNiO_3$ and HgO were also measured at the respective Ti-*L*, Pb-*L* and Hg-*L* edges as reference materials.

Permittivity and ferroelectricity characterization. The permittivity was measured with different frequency by an Agilent-4980A LCR meter on a solid pellet with 4.0 mm in diameter and 230 μm in thickness. The ferroelectric hysteresis loops were measured at 20 Hz with a Radiant Precision Premier-II Ferroelectric Test System at different temperatures based on the proposed positive-up negative-down (PUND) method. Detailed experimental descriptions can be found in Ref. [20].

Data availability

The data that support the findings of this study are available from the corresponding authors upon reasonable request.

Received: 30 August 2020; Accepted: 22 December 2020;
Published online: 02 February 2021

References

1. Goodenough, J. & Longo, J. Crystallographic and magnetic properties of perovskite and perovskite related compounds. Landolt-Bornstein Numerical Data and Functional Relationships in Science and Technologym, eds Hellwege, K.-H., Hellwege, A. M. (Springer, Berlin) III/4, 126–314 (1970).
2. Hayward, M. A. et al. The hydride anion in an extended transition metal oxide array: $LaSrCoO_3H_{0.7}$. *Science* **295**, 1882–1884 (2002).
3. Jin, C. Q. et al. Superconductivity at 80 K in $(Sr,Ca)_3Cu_2O_4+_\delta Cl_2$-y induced by apical oxygen doping. *Nature* **375**, 301–303 (1995).
4. Zhang, J. J. et al. Large orbital polarization in a metallic square-planar nickelate. *Nat. Phys.* **13**, 864–870 (2017).
5. Li, M. R. et al. $Mn_2(Fe_{0.8}Mo_{0.2})MoO_6$: a double perovskite with multiple transition metal sublattice magnetic effects. *Chem. Mater.* **30**, 4508–4514 (2018).
6. Lin, J. F. et al. Spin transition zone in Earth's lower mantle. *Science* **317**, 1740–1743 (2007).
7. Kageyama, H. et al. Expanding frontiers in materials chemistry and physics with multiple anions. *Nat. Commun.* **9**, 772 (2018).
8. Li, W. M. et al. Superconductivity in a unique type of copper oxide. *Proc. Natl Acad. Sci. USA* **116**, 12156–12160 (2019).
9. Jin, C. Q., Adachi, S., Wu, X. J., Yamauchi, H. & Tanaka, S. 117 K Superconductivity in the Ba-Ca-Cu-O system. *Phys. C.* **223**, 238–242 (1994).
10. Shimakawa, Y. A-site-ordered perovskites with intriguing physical properties. *Inorg. chem.* **47**, 8562–8570 (2008).
11. Zeng, Z., Greenblatt, M., Subramanian, M. A. & Croft, M. Large low-field magnetoresistance in perovskite-type $CaCu_3Mn_4O_{12}$ without double exchange. *Phys. Rev. Lett.* **82**, 3164–3167 (1999).
12. Yamada, I. et al. A perovskite containing quadrivalent iron as a charge-disproportionated ferrimagnet. *Angew. Chem. Int. Ed.* **47**, 7032–7035 (2008).
13. Ramirez, A. P. et al. Giant dielectric constant response in a copper-titanate. *Solid State Commun.* **115**, 217–220 (2000).
14. Arbatti, M., Shan, X. & Cheng, Z. Y. Ceramic-polymer composites with high dielectric constant. *Adv. Mater.* **19**, 1369–1372 (2007).
15. Cheng, J. G. et al. Possible Kondo physics near a metal-insulator crossover in the A-site ordered perovskite $CaCu_3Ir_4O_{12}$. *Phys. Rev. Lett.* **111**, 176403 (2013).
16. Panda, P. K. Review: environmental friendly lead-free piezoelectric materials. *J. Mater. Sci.* **44**, 5049–5062 (2009).
17. Belik, A. A. et al. Low-temperature structural modulations in $CdMn_7O_{12}$, $CaMn_7O_{12}$, $SrMn_7O_{12}$, and $PbMn_7O_{12}$ perovskites studied by synchrotron X-ray powder diffraction and mossbauer spectroscopy. *J. Phys. Chem. C.* **120**, 8278–8288 (2016).
18. Jin, C. Q. et al. High-pressure synthesis of the cubic perovskite BaRuO3 and evolution of ferromagnetism in ARuO3 (A = Ca, Sr, Ba) ruthenates. *Proc. Natl Acad. Sci. USA* **105**, 7115–7119 (2008).
19. Deng, H. S. et al. Strong enhancement of spin ordering by A-site magnetic ions in the ferrimagnet $CaCu_3Fe_2Os_2O_{12}$. *Phys. Rev. B* **94**, 024414 (2016).
20. Zhou, L. et al. Realization of large electric polarization and strong magnetoelectric coupling in $BiMn_3Cr_4O_{12}$. *Adv. Mater.* **29**, 1703435 (2017).
21. Long, Y. W. et al. Temperature-induced A-B intersite charge transfer in an A-site-ordered $LaCu_3Fe_4O_{12}$ perovskite. *Nature* **458**, 60–63 (2009).
22. Wang, X. et al. Observation of magnetoelectric multiferroicity in a cubic perovskite system: $LaMn_3Cr_4O_{12}$. *Phys. Rev. Lett.* **115**, 087601 (2015).
23. Yamada, I. et al. Control of bond-strain-induced electronic phase transitions in iron perovskites. *Inorg. Chem.* **52**, 13751–13761 (2013).
24. Yin, Y. Y. et al. $LaMn_3Ni_2Mn_2O_{12}$: An A- and B-site ordered quadruple perovskite with A-site tuning orthogonal spin ordering. *Chem. Mater.* **28**, 8988–8996 (2016).
25. Long, Y. et al. Intermetallic charge transfer in A-site-ordered double perovskite $BiCu_3Fe_4O_{12}$. *Inorg. Chem.* **48**, 8489–8492 (2009).
26. Choi, K. J. et al. Enhancement of ferroelectricity in strained $BaTiO_3$ thin films. *Science* **306**, 1005–1009 (2004).
27. Kubel, F. & Schmid, H. Structure of a ferroelectric and ferroelastic monodomain crystal of the perovskite $BiFeO_3$. *Acta Crystallogr. B* **46**, 698–702 (1990).
28. Aimi, A. et al. High-pressure synthesis of A-site ordered double perovskite $CaMnTi_2O_6$ and ferroelectricity driven by coupling of A-site ordering and the second-order Jahn-Teller effect. *Chem. Mater.* **26**, 2601–2608 (2014).
29. Sawaguchi, E. Ferroelectricity versus antiferroelectricity in the solid solutions of $PbZrO_3$ and $PbTiO_3$. *J. Phys. Soc. Jpn.* **8**, 615–629 (1953).
30. Yamamoto, T. Ferroelectric properties of the $PbZrO_3$-$PbTiO_3$ system. *Jpn. J. Appl. l Phys.* **35**, 5104–5108 (1996).
31. Johnson, R. D. et al. Giant improper ferroelectricity in the ferroaxial magnet $CaMn_7O_{12}$. *Phys. Rev. Lett.* **108**, 067201 (2012).
32. Belik, A. A. et al. Spin-driven multiferroic properties of $PbMn_7O_{12}$ perovskite. *Inorg. Chem.* **55**, 6169–6177 (2016).
33. Mezzadri, F. et al. Synthesis and characterization of multiferroic $BiMn_7O_{12}$. *Phys. Rev. B* **79**, 100106 (R) (2009).
34. Ovsyannikov, S. V. et al. Structural and magnetic transitions in CaCo3V4O12 perovskite at extreme conditions. *Inorg. Chem.* **56**, 6251–6263 (2017).
35. Leinenweber, K., Linton, J., Navrotsky, A., Fei, Y. & Parise, J. B. High-pressure perovskites on the join $CaTiO_3$-$FeTiO_3$. *Phys. Chem. Miner.* **22**, 251–258 (1995).
36. Shiro, K. et al. Pd^{2+}-incorporated perovskite $CaPd_3B_4O_{12}$ (B = Ti, V). *Inorg. Chem.* **52**, 1604–1609 (2013).
37. Orgel, L. E. & Dunitz, J. D. Stereochemistry of cupric compounds. *Nature* **179**, 462–465 (1957).
38. De Groot, F. X-ray absorption and dichroism of transition metals and their compounds. *J. Electron. Spectrosc.* **67**, 529–622 (1994).
39. Schlappa, J. et al. Resonant soft x-ray scattering from stepped surfaces of $SrTiO_3$. *J. Phys.-Condens. Mat.* **24**, 035501 (2012).
40. Gegner, J. et al. Insulator-metal transition in TiGePt: a combined photoelectron spectroscopy, x-ray absorption spectroscopy, and band structure study. *Phys. Rev. B* **85**, 235106 (2012).
41. Haverkort, M. W. et al. Determination of the orbital moment and crystal-field splitting in $LaTiO_3$. *Phys. Rev. Lett.* **94**, 056401 (2005).
42. Chang, C. F. et al. c-axis dimer and its electronic breakup: the insulator-to-metal transition in Ti_2O_3. *Phys. Rev. X* **8**, 021004 (2018).
43. Degroot, F. M. F., Fuggle, J. C., Thole, B. T. & Sawatzky, G. A. $L_{2,3}$ X-ray-absorption edges of d^0 compounds: K^+, Ca^{2+}, Sc^{3+} and Ti4$^+$ in Oh (octahedral) symmetry. *Phys. Rev. B* **41**, 928–937 (1990).
44. Pichler, T. et al. Proof for trivalent Sc ions in Sc_2 @ C_{84} from high-energy spectroscopy. *Phys. Rev. B* **62**, 13196–13201 (2000).
45. Yamanaka, T., Hirai, N. & Komatsu, Y. Structure change of $Ca_{1-x}Sr_xTiO_3$ perovskite with composition and pressure. *Am. Mineral.* **87**, 1183–1189 (2002).
46. Chen, K. et al. Valence state of Pb in transition metal perovskites $PbTMO_3$ (TM = Ti, Ni) determined from X-ray absorption near-edge spectroscopy. *Phys. Status Solidi B* **255**, 1800014 (2018).
47. Zhu, J. L. et al. Nuclear and charge density distributions in ferroelectric PbTiO3: maximum entropy method analysis of neutron and X-ray diffraction data. *Powder Diffr.* **28**, 276–280 (2013).
48. Lebeugle, D., Colson, D., Forget, A. & Viret, M. Very large spontaneous electric polarization in $BiFeO_3$ single crystals at room temperature and its evolution under cycling fields. *Appl. Phys. Lett.* **91**, 022907 (2007).
49. Wang, Y. P., Yuan, G. L., Chen, X. Y., Liu, J. M. & Liu, Z. G. Electrical and magnetic properties of single-phased and highly resistive ferroelectromagnet $BiFeO_3$ ceramic. *J. Phys. D. Appl. Phys.* **39**, 2019–2023 (2006).
50. Lebeugle, D. et al. Room-temperature coexistence of large electric polarization and magnetic order in $BiFeO_3$ single crystals. *Phys. Rev. B* **76**, 024116 (2007).
51. Zhang, J. et al. A new quasi-one-dimensional compound Ba_3TiTe_5 and superconductivity induced by pressure. *NPG Asia Mater.* **11**, 60 (2019).
52. Deng, Z. et al. A pressure-induced inverse order-disorder transition in double perovskites. *Angew. Chem. Int. Ed.* **59**, 8240–8246 (2020).
53. Toby, B. H. EXPGUI, a graphical user interface for GSAS. *J. Appl. Crystallogr* **34**, 210–213 (2001).

Acknowledgements

The work was supported by National Science Foundation and Ministry of Science and Technology of China through the research projects (2018YFA0305700, 11921004, 11820101003, U2032220, 2017YFA0302900), and Beijing Nature Science Foundation (2202059).

Author contributions

C.Q.J. conceived and supervised the project. C.Q.J., R.Z.Y., and H.M.W. coordinated the research. J.F.Z., X.W., W.M.L., J.Z., Z.D., L.D., C.W.R., Y.W.L., J.L.Z., R.Z.Y. and X.C.W. synthesized the samples and performed the major measurements. X.D.S., J.F.Z. and Y.W. L. carried out the dielectric and ferroelectric measurements with the help of others. J.F.Z., Y.R., R.Z.Y., C.Q.J. and C.D. performed the X-ray diffraction and crystal structure analysis. Q.Z.H. and J.F.Z. collected the powder neutron diffraction data and carried out the data analysis with the help of others. X.S. and R.C.Y. carried the TEM measurements. J.F.Z., Z.W.H., L.P.C., W.M.L., S.C.W., H.J.L., C.T.C. and L.H.T. carried out the XAS measurements. J.C.G., Y.T.Q., Z.L. and H.M.W. did the theoretical calculations. J.F.Z., R. Z.Y., Q.Q.L., C.Q.J. discussed with M.G. the experimental results in many details. J.F.Z., R.Z.Y. and C.Q.J. wrote the manuscript with comments from H.M.W., M.G. & Z.W.H. All authors contributed to the version.

Competing interests

The authors declare no competing interests.

Additional information

Supplementary information The online version contains supplementary material available at https://doi.org/10.1038/s41467-020-20833-6.

Correspondence and requests for materials should be addressed to H.W., R.Y. or C.J.

Peer review information *Nature Communications* thanks Shiming Zhou and the other, anonymous, reviewer(s) for their contribution to the peer review of this work.

Reprints and permission information is available at http://www.nature.com/reprints

Publisher's note Springer Nature remains neutral with regard to jurisdictional claims in published maps and institutional affiliations.